Research article

Carbon Future

MOF-derived 3D hierarchical porous TiO_2@NPC@S as high-performance cathodes for Li-S batteries

Peng Shi[1,#], Chengyao Zhu[1,#], Chuxin Chen[1], Ying Luo[2], Feng Sun[3], Xuan Du[1], Tao Zhou[1], and Guo Gao[1] ✉

[1] *School of Sensing Science and Engineering, School of Electronic Information and Electrical Engineering, Shanghai Jiao Tong University, Shanghai 200240, China*
[2] *State Key Laboratory of Space Power Sources, Shanghai Institute of Space Power Sources, Shanghai 200245, China*
[3] *School of Materials and Engineering, Shanghai Jiao Tong University, Shanghai 200240, China*

Cite This: *Carbon Future* **2025**, *2*, 9200035

Read Online

ABSTRACT: The capacity of traditional lithium-ion batteries has approached theoretical limits, and exploring lithium-sulfur batteries (LSBs) with high capacity and energy density is highly desired. Metal–organic framework (MOF)-derived materials are among the most crucial candidates for LSBs. The objectives of present work are improving the electrical conductivity, slowing down the volume expansion, and inducing the notorious "shuttle effect". In this work, we developed MOF-derived nanoporous carbon (NPC)-coated composite TiO_2@NPC as ideal sulfur host for Li-S batteries. The NPC offers sufficient space for the expansion of sulfur volume during electrochemical cycling process, while forming a conductive framework to promote the transport of ion and electron. High sulfur loading of 64.09% was obtained through both physical and chemical strategies. The TiO_2@NPC@S cathode with multifunctional effects exhibits outstanding long-term cycling performance, presenting an initial capacity of up to 1327.35 mAh/g at 0.5 C with an average capacity decrease of 0.18% per cycle. It exhibits commendable rate capabilities, achieving 928 mAh/g at 1 C and 743 mAh/g at 1.5 C. The electrochemical performance of the synthesized TiO_2@NPC@S is significant superior to the commercial Y-50@S materials. This work provides a successful approach for designing novel high-performance cathodes in LSBs.

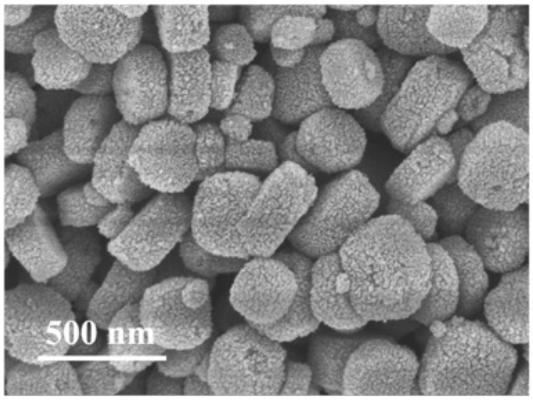

KEYWORDS: lithium-sulfur battery, metal–organic frameworks, sulfur composites

1 Introduction

In recent decades, lithium-ion batteries have gained considerable interests owing to their widespread applications in portable electronic devices and electric cars[1–3]. However, despite the continuous improvement in the performance of lithium-ion batteries in terms of energy and power density, the capacity of traditional cathode electrodes is reaching up to the theoretical limits[4, 5]. Therefore, it is urgent to explore alternative battery materials. Lithium-sulfur batteries (LSBs), possessing outstanding theoretical specific capacity (1675 mAh/g) and high energy density (2500 Wh/kg), are deemed as one of the most promising alternatives for lithium-ion batteries[6–9].

Received: December 18, 2024; **Revised:** January 8, 2025
Accepted: January 15, 2025

✉Address correspondence to guogao@sjtu.edu.cn
#Peng Shi and Chengyao Zhu contributed equally to this work.

https://doi.org/10.26599/CF.2025.9200035

While LSBs have superior performance and low cost, they own inherent shortcomings that impede the further development. Firstly, the intrinsic insulating nature of sulfur and the discharged intermediates of Li_2S_2/Li_2S generate slow redox reactions and non-ideal ion transportation, resulting in poor electrochemical utilization and cycling stability[10–12]. Secondly, the cathode sustains a substantial 80% volume expansion during the conversion of S_8 to Li_2S. This expansion will restrict the cycling life of LSBs by decreasing the damage of the electrode structure during the long-time charging and discharging proccess[13, 14]. Thirdly, arising from the direct exposure of sulfur and its products to the electrolyte, the uncontrollable diffusion of soluble intermediate polysulfides (Li_2S_n, $2 < n \leq 8$) induces the notorious "shuttle effect"[15, 16]. The unexpected result is the self-discharge problem which generates low sulfur utilization and poor energy efficiency.

In order to resolve these challenges, one of the practical strategies is to search for suitable cathode hosts, such as carbon materials[17–20], metal oxides[21, 22], and composites[23–25]. Among them, hybrid cathodes combining sulfur and carbon will be an ideal approach to resolve the poor conductivity[26]. In the matter of porous carbon

materials, it is widely accepted that the big pore volume and large specific surface area could decrease the volume expansion effectively[27]. However, the effect of mitigating the "shuttle effect" of polar polysulfides is decreased via the non-polar carbon surface. Metal oxides possessing polar surface like ZnO[28], Co_4O_3[29], and TiO_2[30, 31] are also applied to establish composite cathodes as hosts. Non-polar bonds of metal oxides easily combinine with sulfur, but they still have limited conductivity. Recently, metal–organic frameworks (MOFs), which are made of metal ions and organic ligands, have been intensively studied[32]. However, the majority of MOFs have poor conductivity that inhibits ion diffusion and electron transport. The MOF-derived materials could offer a "two birds with one stone" method for combining porous carbon materials and metal oxides.

Herein, the three-dimensional (3D) MOF-derived hierarchical porous structure TiO_2@NPC@S (NPC = nanoporous carbon) composites have been developed. The composites possess a special synergistic fixation effect of polysulfide via physical/chemical process. On the other hand, the synthesized 3D TiO_2@NPC composites could improve the storage of active substances and provide sufficient space for inhibiting the volume expansion, while micropores are easy to capture smaller sulfur molecules and enhance the transfer of ions and electrons. The porous carbon could play a role of conductive skeleton and improve the electron transport rate. TiO_2 can be used as a functionalized polar active site for fixing the polysulfides. Compared with commercial Y-50, the synthesized MOF-derived TiO_2@NPC composites exhibit better electrochemical performance.

2 Material and methods

2.1 Synthesis of MOF precursors

The MOF precursor was synthesized by stirring at room temperature and solvent-heating. First, 3 g of phthalic acid ($C_8H_6O_4$) was added to a mixture containing 54 mL of N,N-dimethylformamide (DMF) and 8 mL of methanol. After ultrasonic treatment for 40 min, 1.4 mL of tetrabutyltitanate ($C_4H_{36}O_4Ti$) was added and intensely stirred at room temperature for 60 min. Following rotation, the white, cloudy liquid was placed in a hydrothermal kettle and then heated in a muffle furnace at 155 °C for 20 h. Following this, the sample was cooled to room temperature, washed three times with DMF and methanol, and finally dried in a vacuum oven at 60 °C to obtain the MOF precursor.

2.2 Synthesis of MOF-derived TiO_2@NPC

The prepared MOF precursor material underwent drying in a vacuum oven at 60 °C, then it was transferred into a high-temperature tube furnace, and was carbonized at 500 °C for 12 h under nitrogen atmosphere at a heating rate of 5 °C/min to form black powder, and TiO_2@NPC was achieved after cooling down naturally.

2.3 Synthesis of TiO_2@NPC@S

After thoroughly mixing the obtained TiO_2@NPC material with sublimed sulfur in a mortar, with a mass ratio of 3:7, grinding continued until a homogeneous mixture was achieved. Subsequently, the mixture was vacuum-sealed and transferred to a muffle furnace, where it was heated to 160 °C and maintained for 12 h. The TiO_2@NPC@S composites were obtained after natural cooling to room temperature.

2.4 Preparation of comparison sample Y-50@S

The commercial lithium-sulfur battery cathode material, Y-50, was mixed with sublimed sulfur powder in a mass ratio of 3:7 to ground thoroughly in an agate mortar. Subsequently, the mixed material was sealed in a quartz glass tube filled with argon gas. The sealed quartz glass tube was then transferred into a muffle furnace and maintained at 160 °C for 12 h before naturally cooling down to produce the Y-50@S composite.

2.5 The electrode preparation

The electrode material, conductive carbon black, and polyvinylidene fluoride (PVDF) binder were weighed according to the mass ratio 7:2:1. The dispersant N-methyl-2-pyrrolidone (NMP) was added and stirred for 8–12 h. Then the coater was used to evenly scrape the positive slurry onto the aluminum foil collector, the thickness of the slurry was controlled at 150 μm, and was dried under vacuum at 50 °C for 12 h. The cathode material was made into 12 mm diameter round pieces by a punching machine, and weighed to calculate the mass of the active substance. Finally, the prepared button cells were sealed using a sealing machine with a pressure greater than 50 kg/cm^2. The button cells were allowed to stand for 12 h, ensuring complete contact between all components of the cell before proceeding to electrochemical performance testing.

2.6 Cell preparation

The electrode prepared in the experiment was cathode, the anode was a lithium plate, and the Celgard 2400 PP film was the separator. The electrolyte used a commercial lithium-sulfur electrolyte (8 μL/mg, relative to the active substance) with a composition of $LiTF_6$ (1 M) and lithium nitrates (2%) dissolved in a volume ratio of 1:1 1,3-dioxolane (DOL) and 1,2-dimethoxyethane (DME). The operation was conducted in the glove box, with the partial pressure of water and oxygen lower than 0.1 ppm.

2.7 Characterization

The morphology and structure of the samples were measured by the scanning electron microscopy (SEM; WITec apyron) and the transmission electron microscopy (TEM; Thermo Scientific). X-ray diffraction (XRD; Empyrean, PANalytical) was applied to analyze the crystalline phases of the materials fitted with a Cu Kα radiation source. Thermogravimetric analysis (TGA; STA 449 F3 Jupiter, NETZSCH) was used to analyze the thermal stability of the cathode materials. TiO_2@NPC and TiO_2@NPC@S were heated from room temperature to 500 °C under an Ar atmosphere with a rate of 10 °C/min. Nitrogen adsorption–desorption measurements were conducted with a Micromeritics ASAP 2020 instrument at 77 K. X-ray photoelectron spectroscopy (XPS; Kratos) was used to confirm the chemical composition and formation of the TiO_2@NPC@S composites.

2.8 Electrochemical measurements

2032-type stainless steel coin cells were assembled in an Ar-filled glovebox. The areal mass density of the sulfur in TiO_2@NPC@S cathode was 2.2 mg/cm^2. Electrochemical measurements were conducted using a LAND galvanostatic charge–discharge instrument (CT21001A), with the testing voltage range of 1.4–2.8 V. The testing temperature was set at 25 °C. The cyclic voltammetry (CV) and electrochemical impedance spectroscopy (EIS) tests were performed using CHI600A. The voltage range of

CV was 1.5–2.8 V and the scan rate range was 0.01–0.5 mV/s. EIS was carried out at 5 mV with the frequency range of 0.01–100 kHz.

3 Results and discussion

Fig. 1 and **Fig. 2** show the analysis of SEM and TEM for the morphology, crystal structure, and element distribution of MOF-derived TiO_2@NPC and TiO_2@NPC@S. Fig. 1a presents the SEM image of MOF-derived TiO_2@NPC, revealing particles with a regular 3D pill-structure, with a diameter ranging from 200 to 400 nm and a thickness range of 100 to 150 nm. MOF-derived TiO_2@NPC effectively retains the framework structure of MOFs, maintaining the pill-like morphology with uneven pore structures on the surface. Fig. 1b displays the TEM image of MOF-derived TiO_2@NPC, illustrating the hierarchical structure of nano-sized particles on both the surface and interior, with evident observation of numerous pores within. The hierarchical porous structure forms a mesoporous and microporous architecture, providing space for accommodating more sublimated sulfur and alleviating the volume changes in the course of the charge–discharge processes. Figs. 1c and 1d illustrate the SEM and TEM images of the MOF-derived TiO_2@NPC@S composite material after S storage, respectively. While there is no significant difference in the overall morphology of TiO_2@NPC@S, the microscopic structures on the surface and within reveal notable discrepancies, especially the morphological shift of TiO_2@NPC from a relatively regular pill structure to an irregular assemblage of fragments following sulfur impregnation. This phenomenon can be attributed to two primary mechanisms. The sulfur atoms successively attach to the active sites of TiO_2, inducing stress alterations within the crystal lattice, which leads to the disruption of the initial structural stability and subsequent collapse and reorganization of the surface architecture. Additionally, as sulfur diffuses into the interior of NPC pores, the heterogeneous distribution of sulfur within the pores generates local stress concentrations, rendering the NPC structure more susceptible to fracturing and contributing to the overall structural transformation. In comparison with the TiO_2@NPC material with evident pore structures in Fig. 1a, Fig. 1c shows that the pores in TiO_2@NPC@S composite material appear visibly filled, suggesting that sublimated sulfur has diffused and been immobilized within the pores of TiO_2@NPC. Fig. 1d further elucidates that the distinct pore structures observed in the TEM image of TiO_2@NPC material in Fig. 1b disappear after sulfur storage. The TiO_2@NPC@S composite material exhibits a denser internal structure without apparent voids.

As shown in Fig. 2a, in high-resolution TEM (HRTEM) lattice image, distinct lattice spacings of 0.37 nm are prominently noticed, corresponding to the (101) plane of TiO_2[33]. This observation suggests excellent crystallinity of TiO_2 within the MOF-derived TiO_2@NPC composite material, which facilitates enhancing the structural stability of the electrode material. Fig. 2b presents the local electron diffraction pattern of the TiO_2@NPC@S composite material. Notably, high-resolution concentric rings with bright central spots are discernible in the local diffraction pattern, affirming the polycrystalline nature of the TiO_2@NPC@S. The main concentric rings in Fig. 2b are distributed outward on the anatase phase of TiO_2 (200), (004), and (101) planes[34], indicating the successful preparation of MOF-derived anatase TiO_2@NPC@S composites. To validate the storage of S, elemental scanning analysis was conducted on the TiO_2@NPC@S composites, as illustrated in Figs. 2c–2g. As is evident, sulfur elements are uniformly distributed within the TiO_2@NPC@S composites, exhibiting a relatively dense distribution. This observation confirms the creation of a homogeneous composite materials, with sulfur tightly integrated with the TiO_2@NPC material.

To confirm the composition of the synthesized material, XRD tests were conducted on the prepared samples. **Fig. 3a** illustrates the XRD diffraction spectra of sulfur, MOF-derived TiO_2@NPC, and TiO_2@NPC@S composites. The XRD pattern of the obtained TiO_2@NPC exhibits a characteristic anatase structure, in agreement

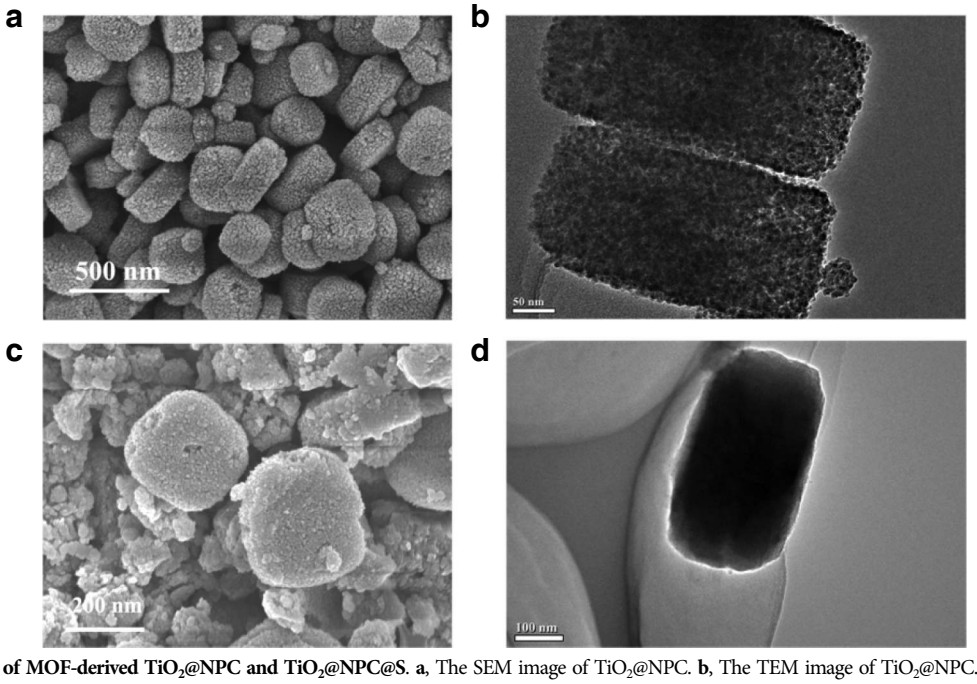

Fig. 1. Morphologies of MOF-derived TiO_2@NPC and TiO_2@NPC@S. a, The SEM image of TiO_2@NPC. **b**, The TEM image of TiO_2@NPC. **c**, The SEM image of TiO_2@NPC@S. **d**, The TEM image of TiO_2@NPC@S.

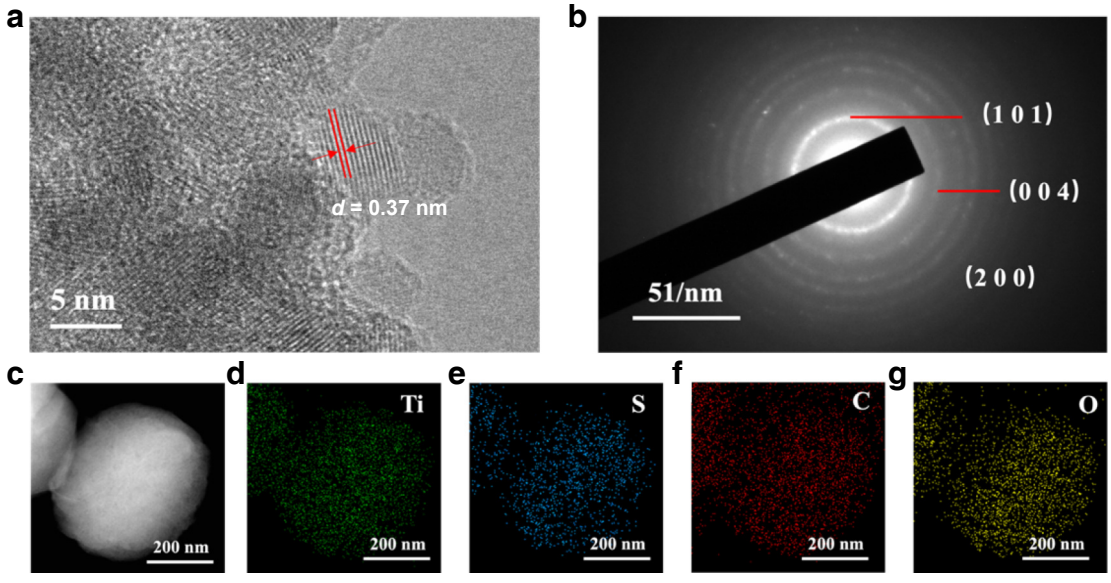

Fig. 2. Crystal structure and element distribution diagram of MOF-derived TiO_2@NPC and TiO_2@NPC@S. a, The HRTEM diagram of TiO_2@NPC. **b**, The selected area electron diffraction (SAED) diagram of TiO_2@NPC@S. **c**–**g**, The element distribution diagrams of TiO_2@NPC@S.

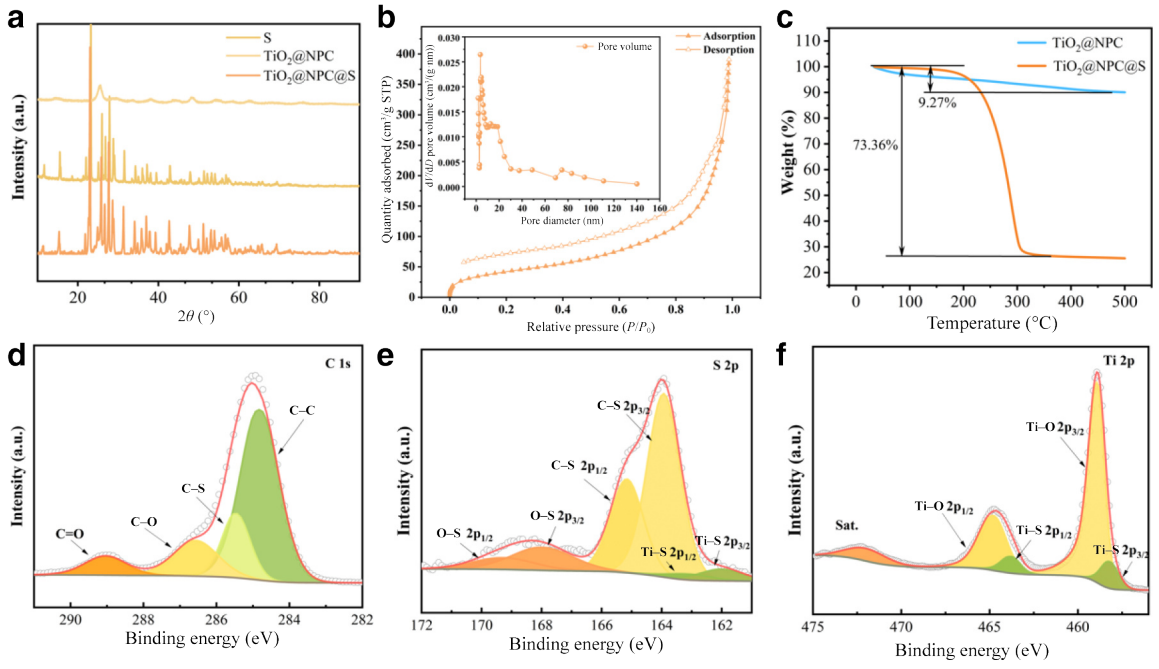

Fig. 3. Composition, property, and chemical state analysis of MOF-derived TiO_2@NPC and TiO_2@NPC@S composites. a, XRD diffraction patterns of MOF-derived TiO_2@NPC and TiO_2@NPC@S composites. **b**, Nitrogen adsorption–desorption isotherm and BJH pore size distribution curve of MOF-derived TiO_2@NPC. **c**, TG patterns of MOF-derived TiO_2@NPC and TiO_2@NPC@S composites. **d**–**f**, XPS spectra of TiO_2@NPC@S composites.

with the standard card (JCPDS No. 21-1272)[34]. In the XRD pattern of TiO_2@NPC@S, the sulfur-related diffraction peaks appear notably weak, indicating poor crystallinity. This suggests that sulfur is dispersed and immobilized within the porous TiO_2@NPC. XPS was employed for further elemental state analysis of the TiO_2@NPC@S composites, as depicted in Figs. 3d–3f. Fig. 3e illustrates the narrow XPS spectrum of S 2p in the TiO_2@NPC@S. The two fitted peaks at 165.3 and 164.5 eV are associated with the spin-orbit coupling-induced $2p_{1/2}$ and $2p_{3/2}$ of S, respectively. The electron binding energy positions correspond to the $2p_{3/2}$ and $2p_{1/2}$ of C–S[35]. Fig. 3f delineates the 2p spectrum of Ti, revealing two major peaks at 463.1 and 465.2 eV, which are assigned to $2p_{1/2}$ and $2p_{3/2}$ of Ti, respectively[35]. It indicates that Ti^{4+} in the anatase phase of TiO_2 is in a normal state. The formation of O–S bonds and a small amount of Ti–S suggests that the TiO_2@NPC@S composite material exhibits a robust chemical anchoring effect on S, capable of suppressing the shuttle effect in LSBs and enhancing cycling stability. Following the blending of MOF-derived TiO_2@NPC with sublimed sulfur, sulfur adopted a liquid state at a high temperature of 160 °C, exhibiting the lowest viscosity. This facilitated the facile penetration of sulfur into the porous structure of the host material or its adhesion to the surface, consequently yielding the

TiO_2@NPC@S composite material. To determine the content of the active substance S in the composite material, both MOF-derived TiO_2@NPC and TiO_2@NPC@S materials underwent thermogravimetric (TG) analysis in the nitrogen atmosphere. As illustrated in Fig. 3c, MOF-derived TiO_2@NPC experienced 9.27% weight loss during the heating process up to 500 °C, possibly attributed to the volatilization of residual organic solvents. In contrast, TiO_2@NPC@S exhibited a weight loss of 73.36%, and deducting the intrinsic loss revealed that the S component stored in the TiO_2@NPC@S composite material through physical storage was approximately 64.09%.

Nitrogen adsorption–desorption tests were conducted to further explore the pore structure properties of the TiO_2@NPC material. As illustrated in Fig. 3b, the adsorption curve of TiO_2@NPC displays type IV isotherm with an arresting hysteresis loop, pointing to a typical multi-level pore structure comprising a combination of mesopores and micropores. The non-closure of the nitrogen adsorption–desorption curve results from the complex pore structure. Nitrogen in the pores faces greater desorption resistance, causing incomplete desorption and preventing the curve from returning to its starting position. The Brunauer–Emmett–Teller (BET) calculation revealed an excellent specific surface area of 155.34 m^2/g for TiO_2@NPC. This large surface area could enhance electrolyte infiltration, augmenting the contact area between the TiO_2@NPC material and Li^+. Consequently, it improves the ion migration rate of the electrode material and effectively contributes to the enhancement of rate performance. The pore size distribution of TiO_2@NPC was illustrated by the Barrett–Joyner–Halenda (BJH) pore size distribution curve. It is evident that the TiO_2@NPC material contains a significant quantity of mesopores, in addition to macropores and micropores. The BJH adsorption average pore diameter of TiO_2@NPC is 16.17 nm, and the desorption average pore diameter is 13.40 nm. Given that the diameter of the active material S_8 is 0.68 nm, this implies that macropores are advantageous for storing the active material, hence enhancing the capacity of LSBs[36]. Simultaneously, for the duration of battery cycling, mesopores can adapt to the volumetric expansion of active materials, while micropores effectively restrict the shuttle of polysulfides[37]. The multi-level pore structure and interconnected conductive framework of TiO_2@NPC can facilitate ion and electron transport, providing sufficient space to confine the diffusion of soluble polysulfides, thereby improving the overall performance of electrode.

Fig. 4a illustrates the charge–discharge curves of the TiO_2@NPC@S electrode at 0.5 C. The electrochemical behavior reveals characteristic double-plateau wave features, exhibiting a persistent charging plateau and two discharging plateaus. These features correspond to the oxidation peak and two reduction peaks observed in the CV curve, as shown in Fig. 4b. Specifically, the front one discharge plateau corresponds to the transformation of the active material S into soluble polysulfides, while the second discharge plateau indicates the liquid–solid transformation of soluble polysulfides into insoluble polysulfides and the final products. The reaction in the second stage is relatively slower. Consequently, the TiO_2@NPC@S electrode exhibits a longer second discharge plateau, indicating a more thorough liquid–solid transformation.

Upon examining the charge–discharge curves of the initial cycles, it can be seen that the charge–discharge plateaus of the TiO_2@NPC@S electrode consistently overlap. This observation suggests excellent cycling performance with no significant polarization. However, a rapid decay is noticeable in the first 10 cycles, attributed to the inherent characteristics of the NPC material. Notably, the TiO_2@NPC@S electrode demonstrates lower overvoltage, indicating rapid reaction kinetics at high current densities. Fig. 4b depicts the CV curves of the TiO_2@NPC@S electrode with scan rates of 0.1, 0.2, 0.3, and 0.4 mV/s, within scan voltage range of 1.5 to 2.8 V. It is evident that the MOF-derived

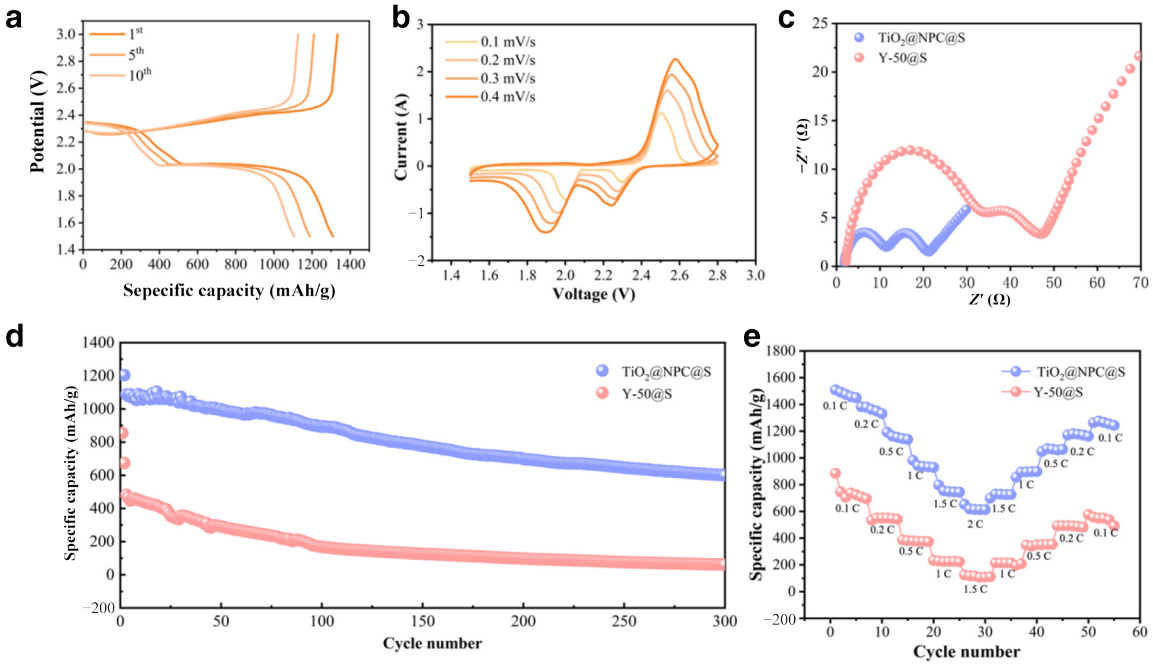

Fig. 4. Electrochemical performance analysis of TiO_2@NPC@S cathodes. a, Galvanostatic charge–discharge curves of TiO_2@NPC@S cathodes. **b**, The CV curves of the TiO_2@NPC@S cathodes under four different scan rates. **c**, EIS spectra of TiO_2@NPC@S and comparison sample Y-50@S. **d**, Cycle-life performance and Coulombic efficiency of TiO_2@NPC@S and Y-50@S at 0.2 C. **e**, Rate performance curves of TiO_2@NPC@S and comparison sample Y-50@S.

TiO_2@NPC@S electrode exhibits two reduction peaks at about 1.8–2.0 V and 2.2–2.3 V, along with a distinct oxidation peak among 2.5–2.6 V. The oxidation peak is notable for its sharp shape, and its amplitude gradually increases with the rising scan rate. The two reduction peaks maintain their original shapes, and their amplitudes steadily increase with higher scan rates, indicating favorable redox reactions. Additionally, on the right side of the oxidation peak and on the left side of the reduction peak at 2.2–2.3 V, additional minor protrusions are observed, attributed to the insertion/extraction of lithium ions from the TiO_2 material.

To further validate the electrochemical performance, MOF-derived TiO_2@NPC@S and the current commercial material Y-50@S were simultaneously employed as cathodes in a comparative experiment. The cycle-life performance curves at 0.2 C for TiO_2@NPC@S and Y-50@S serving as hosts for sulfur are illustrated in Fig. 4d. It is evident that the specific capacity of the commercial material Y-50@S has decayed to below 168.16 mAh/g after 100 cycles, whereas the TiO_2@NPC@S cathode remains 897.49 mAh/g, showcasing a significant advantage. After 300 cycles, the specific capacity of TiO_2@NPC@S still preserves at 601.54 mAh/g (with a decay rate of only 0.16%), while the capacity of commercial material Y-50@S is nearly zero. This phenomenon can be ascribed to the multi-level pore structure of TiO_2@NPC@S, which increases the contact area, and enhances the number of active sites for sulfur and polysulfides immobilization, and the enveloping carbon layer also improves conductivity, enhancing electron transport capability. Therefore, TiO_2@NPC@S exhibits a clear superiority over commercial Y-50@S in terms of cycling life and capacity retention. The rate performance of the two electrodes is depicted in Fig. 4e. At rates of 0.1, 0.2, 0.5, 1, and 1.5 C, the capacities of the TiO_2@NPC@S electrode are 1450, 1331, 1138, 928, and 743 mAh/g, respectively. By contrast, under identical conditions, the discharge capacity of the commercial Y-50@S electrode is lower, and its stability is poorer. For the Y-50@S electrode, at rates above 0.5 C, the capacity begins to drop below 400 mAh/g, reaching almost zero at 1.5 C. After returning to 0.1 C, the capacity is only 500 mAh/g. This indicates that the current commercial Y-50@S electrode lacks the ability for rapid charge and discharge. By contrast, the TiO_2@NPC@S electrode achieves a capacity of 1242 mAh/g after returning to 0.1 C, demonstrating outstanding rate performance. This is ascribed to the high conductivity of NPC, providing an interconnected conductive framework that facilitates rapid electron transport. The increased contact area to accommodate volume expansion, promoted by the stable structure of TiO_2 combined with the multi-level pore structure of TiO_2@NPC, facilitates rapid ion transport.

The EIS tests of TiO_2@NPC@S and commercial Y-50@S cathode were performed. As depicted in Fig. 4c, EIS spectra comprise two semicircles in the high-frequency range and a straight line in the low-frequency range. These two concave semicircles in the high-frequency and mid-high-frequency ranges correspond to the charge transfer resistance at the interface (R_{ct}) and the charge transfer resistance of the electrode–electrolyte membrane solid electrolyte interphase (SEI) film (R_{SEI}), respectively, while the straight line in the low-frequency range corresponds to Li^+ diffusion. These two semicircles indicate the deposition of insoluble Li_2S/Li_2S_2 on electrode surface, forming the electrode–electrolyte membrane SEI film during the cycling process. Although R_{SEI} films are formed on the surfaces of both positive electrodes, the R_{SEI} of TiO_2@NPC@S is significantly smaller than that of the Y-50@S, indicating a substantial mitigation of the deposition of insoluble Li_2S/Li_2S_2 and the shuttle effect on the TiO_2@NPC@S electrode surface. On the other hand, the formation of chemical bonds Ti–S and S–O also reduces resistance at the sulfur-TiO_2@NPC interface. The R_{ct} serves as an indicator of the reaction kinetics in the battery. The R_{ct} of the TiO_2@NPC@S electrode (13 Ω) is significantly lower than the reference sample Y-50@S, which has an R_{ct} of 36 Ω. This is attributed to the multi-level pore structure of the TiO_2@NPC in TiO_2@NPC@S, which shortens the paths for electron and ion transfer. The conductive network framework formed by TiO_2@NPC effectively reduces the charge transfer resistance, and enhances the conductivity and charge transfer rate of the composite electrode, thereby improving the cycling performance of LSBs. This aligns with findings from the preceding cycling and rate performance tests.

4 Conclusions

In summary, we prepared the MOF-derived TiO_2@NPC material with hierarchical porous structure, and further synthesized the TiO_2@NPC@S cathode with high sulfur loading. Morphological characterization revealed the porous structure of the synthesized TiO_2@NPC, demonstrating that the titanium-based oxide in the TiO_2@NPC composite material is a rutile-type TiO_2 with low volume expansion. Nitrogen sorption tests confirmed its unique multi-level pore structure, comprising micro-, meso-, and macropores, shortening the ion transport paths, facilitating rapid ion transfer, and providing sufficient space for sulfur volume expansion during storage and cycling process. The encapsulation of NPC forms a conductive framework within the multi-level pore structure, promoting electron transport in various aspects, leading to exceptional electrochemical performance and cycling stability of the TiO_2@NPC@S electrode. TiO_2 possesses hydrophilic groups (Ti–O) and polar surface hydroxyl groups. Polar–polar chemical bonds are formed in TiO_2@NPC@S, allowing for chemical immobilization of polysulfides, decreasing the interface resistance, and effectively alleviating the shuttle effect. Comparative tests were conducted using TiO_2@NPC@S and the commercial Y-50@S as cathodes for LSBs. Electrochemical results demonstrated that the MOF-derived TiO_2@NPC@S with multifunctional effects exhibited significant advantages in terms of cycling life, rate performance, and electrochemical kinetics. The TiO_2@NPC@S cathode showed an extended cycling life of 300 cycles, with an initial capacity of 1327.35 mAh/g and an average capacity decay of 0.18% per cycle. It exhibited good rate capabilities of 928 and 743 mAh/g at 1 and 1.5 C, respectively. This work provides a new approach to the design of cathodes for LSBs.

References

[1] Assat, G.; Tarascon, J. M. Fundamental understanding and practical challenges of anionic redox activity in Li-ion batteries. *Nat. Energy* **2018**, *3*, 373–386.

[2] Patel, M.; Mishra, K.; Banerjee, R. Chaudhari, J.; Kanchan, D. K.; Kumar, D. Fundamentals, recent developments and prospects of lithium and non-lithium electrochemical rechargeable battery systems. *J. Energy Chem.* **2023**, *81*, 221–259.

[3] Zeng, S. B.; Li, L. G.; Xie, L. H.; Zhao, D. K.; Zhou, N.; Wang, N.; Chen, S. W. Graphene-supported highly crosslinked organosulfur nanoparticles as cathode materials for high-rate, long-life lithium-sulfur battery. *Carbon* **2017**, *122*, 106–113.

[4] Li, M.; Lu, J.; Chen, Z. W.; Amine, K. 30 years of lithium-ion batteries. *Adv. Mater.* **2018**, *30*, 1800561.

[5] Chen, Y. Q.; Kang, Y. Q.; Zhao, Y.; Wang, L.; Liu, J. L.; Li, Y. X.; Liang, Z.; He, X. M.; Li, X.; Tavajohi, N. et al. A review of lithium-ion battery safety concerns: The issues, strategies, and testing standards. *J. Energy Chem.* **2021**, *59*, 83–99.

[6] Deng, R. Y.; Yu, H. Y.; Liu, J. M.; Chu, F. L.; Lei, J.; Yang, L. Z.; Wu, F. X. Adsorption-catalytic effects of metallurgical ferrous slag on polysulfides in Li-S batteries. *J. Mater. Chem. A* **2023**, *11*, 15769–15777.

[7] Zhao, E. Y.; Nie, K. H.; Yu, X. Q.; Hu, Y. S.; Wang, F. W.; Xiao, J.; Li, H.; Huang, X. J. Advanced characterization techniques in promoting mechanism understanding for lithium-sulfur batteries. *Adv. Funct. Mater.* **2018**, *28*, 1707543.

[8] Chen, Y.; Wang, T. Y.; Tian, H. J.; Su, D. W.; Zhang, Q.; Wang, G. X. Advances in lithium-sulfur batteries: From academic research to commercial viability. *Adv. Mater.* **2021**, *33*, 2003666.

[9] Deng, R. M.; Ke, B. Y.; Xie, Y. H.; Cheng, S. L.; Zhang, C. C.; Zhang, H.; Lu, B. G.; Wang, X. H. All-solid-state thin-film lithium-sulfur batteries. *Nano-Micro Lett.* **2023**, *15*, 73.

[10] Luo, Y. F.; Fang, Z. H.; Duan, S. R.; Wu, H. C.; Liu, H. T.; Zhao, Y. X.; Wang, K.; Li, Q. Q.; Fan, S. S.; Zheng, Z. J. et al. Direct monitoring of Li_2S_2 evolution and its influence on the reversible capacities of lithium-sulfur batteries. *Angew. Chem., Int. Ed.* **2023**, *62*, e202215802.

[11] Jin, Z. S.; Lin, T. N.; Jia, H. F.; Liu, B. Q.; Zhang, Q.; Li, L.; Zhang, L. Y.; Su, Z. M.; Wang, C. G. Expediting the conversion of Li_2S_2 to Li_2S enables high-performance Li-S batteries. *ACS Nano* **2021**, *15*, 7318–7327.

[12] Huang, Z. D.; Fang, Y. W.; Yang, M. T.; Yang, J. K.; Wang, Y. Z.; Wu, Z.; Du, Q. C.; Masese, T.; Liu, R. Q.; Yang, X. S. et al. Sulfur in mesoporous tungsten nitride foam blocks: A rational lithium polysulfide confinement experimental design strategy augmented by theoretical predictions. *ACS Appl. Mater. Interfaces* **2019**, *11*, 20013–20021.

[13] Ng, S. F.; Lau, M. Y. L.; Ong, W. J. Lithium-sulfur battery cathode design: Tailoring metal-based nanostructures for robust polysulfide adsorption and catalytic conversion. *Adv. Mater.* **2021**, *33*, 2008654.

[14] Kang, H.; Shin, J.; Kim, T. H.; Lee, Y.; Lee, D.; Lee, J.; Kim, G.; Cho, E. Metal-organic framework-derived magnesium oxide@carbon interlayer for stable lithium-sulfur batteries. *ACS Sustain. Chem. Eng.* **2023**, *11*, 1344–1354.

[15] Li, B. R.; Zhang, T. P.; Song, Z. H.; Jiang, W. Y.; Yang, J. P.; Pei, M. F.; Mao, R. Y.; Jian, X. G.; Hu, F. Y. 3D adsorption-mediator network polymer binders improve redox kinetics and flame retardant performance for high loading lithium-sulfur batteries. *Adv. Funct. Mater.* **2023**, *33*, 2306990.

[16] Chen, Y.; Gao, X. C.; Su, D. W.; Wang, C. Y.; Wang, G. X. Accelerating redox kinetics of lithium-sulfur batteries. *Trends Chem.* **2020**, *2*, 1020–1033.

[17] Yan, M.; Chen, H.; Yu, Y.; Zhao, H.; Li, C. F.; Hu, Z. Y.; Wu, P.; Chen, L. H.; Wang, H. E.; Peng, D. L. et al. 3D ferroconcrete-like aminated carbon nanotubes network anchoring sulfur for advanced lithium-sulfur battery. *Adv. Energy Mater.* **2018**, *8*, 1801066.

[18] Ye, C.; Zhang, L.; Guo, C. X.; Li, D. D.; Vasileff, A.; Wang, H. H.; Qiao, S. Z. A 3D hybrid of chemically coupled nickel sulfide and hollow carbon spheres for high performance lithium-sulfur batteries. *Adv. Funct. Mater.* **2017**, *27*, 1702524.

[19] Lv, C. S.; Cao, H. L.; Deng, W.; Zhao, M.; Miao, Y. Q.; Guo, C. L.; Liu, P. Z.; Wu, Y. C. Carbon nanotube-embedded hollow carbon nanofibers as efficient hosts for advanced lithium-sulfur batteries. *Dalton Trans.* **2023**, *52*, 4700–4707.

[20] Wang, Y. K.; Zhang, R. F.; Pang, Y. C.; Chen, X.; Lang, J. X.; Xu, J. J.; Xiao, C. H.; Li, H. L.; Xi, K.; Ding, S. J. Carbon@titanium nitride dual shell nanospheres as multi-functional hosts for lithium sulfur batteries. *Energy Storage Mater.* **2019**, *16*, 228–235.

[21] Jeon, Y.; Lee, J.; Jo, H.; Hong, H.; Lee, L. Y. S.; Piao, Y. Z. Co/Co_3O_4-embedded N-doped hollow carbon composite derived from a bimetallic MOF/ZnO core–shell template as a sulfur host for Li–S batteries. *Chem. Eng. J.* **2021**, *407*, 126967.

[22] Wang, B.; Ren, Y. L.; Zhu, Y. L.; Chen, S. W.; Chang, S. Z.; Zhou, X. Y.; Wang, P.; Sun, H.; Meng, X. K.; Tang, S. C. Construction of Co_3O_4/ZnO heterojunctions in hollow N-doped carbon nanocages as microreactors for lithium-sulfur full batteries. *Adv. Sci.* **2023**, *10*, 2300860.

[23] Bao, W. Z.; Su, D. W.; Zhang, W. X.; Guo, X.; Wang, G. X. 3D metal carbide@mesoporous carbon hybrid architecture as a new polysulfide reservoir for lithium-sulfur batteries. *Adv. Funct. Mater.* **2016**, *26*, 8746–8756.

[24] Li, Z. H.; He, Q.; Xu, X.; Zhao, Y.; Liu, X. W.; Zhou, C.; Ai, D.; Xia, L. X.; Mai, L. Q. A 3D nitrogen-doped graphene/TiN nanowires composite as a strong polysulfide anchor for lithium-sulfur batteries with enhanced rate performance and high areal capacity. *Adv. Mater.* **2018**, *30*, 1804089.

[25] Dong, W.; Shi, J. L.; Wang, T. S.; Yin, Y. X.; Wang, C. R.; Guo, Y. G. 3D zinc@carbon fiber composite framework anode for aqueous Zn-MnO_2 batteries. *RSC Adv.* **2018**, *8*, 19157–19163.

[26] Zhou, X. X.; Ma, X. T.; Ding, C. M.; Meng, W. J.; Xu, S. D.; Chen, L.; Duan, D. H.; Liu, S. B. A 3D stable and highly conductive scaffold with carbon nanotubes/carbon fiber as electrode for lithium sulfur batteries. *Mater. Lett.* **2019**, *251*, 180–183.

[27] Pang, S. R.; Liu, Y. X.; Zhang, Z.; Li, Y. X.; Li, C. G.; Shi, Z.; Feng, S. H. 3,5-Bis(trifluoromethyl)benzyl modified triazine-based covalent organic frameworks suppressing the shuttle effect of polysulfides in lithium-sulfur batteries. *New J. Chem.* **2024**, *48*, 16–20.

[28] Yang, R. L.; Du, H. W.; Lin, Z. Q.; Yang, L. L.; Zhu, H.; Zhang, H.; Tang, Z. K.; Gui, X. C. ZnO nanoparticles filled tetrapod-shaped carbon shell for lithium-sulfur batteries. *Carbon* **2019**, *141*, 258–265.

[29] Cheng, H.; Wang, S. P.; Tao, D.; Wang, M. Sulfur/Co_3O_4 nanotube composite with high performances as cathode materials for lithium sulfur batteries. *Funct. Mater. Lett.* **2014**, *7*, 1450020.

[30] Ravikumar, S.; Mani, D.; Khan, M. R.; Ahmad, N.; Sylvestre, S.; Surya, C.; Krishnakumar, B.; Pandiyan, V.; Ahn, Y. H. Ag-TiO_2@Pd/C nanocomposites for efficient degradation of Reactive Red 120 dye and ofloxacin antibiotic under UV and solar light and its antimicrobial activity. *J. Environ. Chem. Eng.* **2021**, *9*, 106657.

[31] Yu, M. P.; Ma, J. S.; Song, H. Q.; Wang, A. J.; Tian, F. Y.; Wang, Y. S.; Qiu, H.; Wang, R. M. Atomic layer deposited TiO_2 on a nitrogen-doped graphene/sulfur electrode for high performance lithium-sulfur batteries. *Energy Environ. Sci.* **2016**, *9*, 1495–1503.

[32] Deng, F. J.; Zhang, Y. H.; Yu, Y. J. Conductive metal-organic frameworks for rechargeable lithium batteries. *Batteries* **2023**, *9*, 109.

[33] Zhou, G. M.; Zhao, Y. B.; Zu, C. X.; Manthiram, A. Free-standing TiO_2 nanowire-embedded graphene hybrid membrane for advanced Li/dissolved polysulfide batteries. *Nano Energy* **2015**, *12*, 240–249.

[34] Huang, Z. H.; Chen, H.; Zhao, L.; He, X.; Fang, W.; Du, Y. Y.; Li, W. X.; Wang, G. H.; Zhang, F. Q. CdSe QDs sensitized MIL-125/TiO_2@SiO_2 biogenic hierarchical composites with enhanced photocatalytic properties via two-level heterostructure. *J. Mater. Sci. Mater. Electron.* **2018**, *29*, 12045–12054.

[35] Ni, J.; Jin, L. M.; Xue, M. Z.; Zheng, J. S.; Zheng, J. P.; Zhang, C. M. TiO_2 microboxes as effective polysufide reservoirs for lithium sulfur batteries. *Electrochim. Acta* **2019**, *296*, 39–48.

[36] Qiu, H. Y.; Song, Y.; Gu, J. H.; Li, Z. Y.; Zheng, J. Q.; Wang, M. R.; Hong, B.; Li, J.; Lai, Y. Q. A bifunctional electrolyte additive ammonium hexafluorophosphate for long cycle life lithium-sulfur batteries. *Mater. Lett.* **2023**, *351*, 134986.

[37] Dong, S. H.; Liu, H. J.; Hu, Y. Z.; Chong, S. K. Cathode materials for rechargeable lithium-sulfur batteries: Current progress and future prospects. *ChemElectroChem* **2022**, *9*, e202101564.

Data availability

All data needed to support the conclusions in the paper are presented in the manuscript. Additional data related to this paper may be requested from the corresponding author upon request.

Acknowledgements

We thank the financial support from the National Key Research and Development Program of China (No. 2022YFA1207503), the Giga Force Electronics Interdisciplinary Funding (No. JJHXM002208-2023), and the Interdisciplinary Program of Shanghai Jiao Tong University (No. YG2025QNB18).

Author contributions

P. S.: writing original draft, investigation, formal analysis, data curation, and methodology. C. Y. Z.: data curation, methodology, validation, writing, review, and editing. C. X. C.: data curation, validation, writing, review, and editing. Y. L.: data curation, resources and validation; F. S.: investigation. X. D.: investigation. T. Z.: investigation. G. G.: conceptualization, funding acquisition, methodology, supervision, writing, review, and editing.

Competing interests

The authors have no competing interests to declare that are relevant to this article.

Use of AI statement

None.